01 Aug 2018

# Fast Prediction Of Thermal Distortion In Metal Powder Bed Fusion Additive Manufacturing: Part 2, A Quasi-static Thermo-mechanical Model

Hao Peng

Morteza Ghasri-Khouzani

Shan Gong

Ross Attardo

*et. al. For a complete list of authors, see https://scholarsmine.mst.edu/mec_aereng_facwork/5186*



## Recommended Citation

H. Peng and M. Ghasri-Khouzani and S. Gong and R. Attardo and P. Ostiguy and R. B. Rogge and B. A. Gatrell and J. Budzinski and C. Tomonto and J. Neidig and M. R. Shankar and R. Billo and D. B. Go and D. Hoelzle, "Fast Prediction Of Thermal Distortion In Metal Powder Bed Fusion Additive Manufacturing: Part 2, A Quasi-static Thermo-mechanical Model," *Additive Manufacturing*, vol. 22, pp. 869 - 882, Elsevier, Aug 2018.

The definitive version is available at https://doi.org/10.1016/j.addma.2018.05.001

Additive Manufacturing 22 (2018) 869–882

Contents lists available at ScienceDirect

Additive Manufacturing

journal homepage: www.elsevier.com/locate/addma

Full Length Article

# Fast prediction of thermal distortion in metal powder bed fusion additive manufacturing: Part 2, a quasi-static thermo-mechanical model

Hao Peng[a,1], Morteza Ghasri-Khouzani[b], Shan Gong[b], Ross Attardo[c], Pierre Ostiguy[c], Ronald B. Rogge[d], Bernice Aboud Gatrell[c], Joseph Budzinski[c], Charles Tomonto[c], Joel Neidig[e], M. Ravi Shankar[b], Richard Billo[f], David B. Go[a,g,*], David Hoelzle[h,**]

[a] Dept. of Aerospace and Mechanical Engineering, University of Notre Dame, United States
[b] Dept. of Industrial Engineering, University of Pittsburgh, United States
[c] Johnson & Johnson Co., United States
[d] Canadian Neutron Beam Centre, Chalk River Laboratories, Canada
[e] ITAMCO, United States
[f] Dept. of Computer Science, University of Notre Dame, United States
[g] Dept. of Chemical and Biomolecular Engineering, University of Notre Dame, United States
[h] Dept. of Mechanical and Aerospace Engineering, The Ohio State University, United States

ARTICLE INFO

*Keywords:*
Additive manufacturing
Powder bed fusion
Direct metal laser sintering
Thermal distortion
Thermal stress
Quasi-Static
Thermo-Mechanical

ABSTRACT

The additive manufacturing (AM) process metal powder bed fusion (PBF) can quickly produce complex parts with mechanical properties comparable to that of wrought materials. However, thermal stress accumulated during Metal PBF may induce part distortion and even cause failure of the entire process. This manuscript is the second part of two companion manuscripts that collectively present a part-scale simulation method for fast prediction of thermal distortion in Metal PBF. The first part provides a fast prediction of the temperature history in the part via a thermal circuit network (TCN) model. This second part uses the temperature history from the TCN to inform a model of thermal distortion using a quasi-static thermo-mechanical model (QTM). The QTM model distinguished two periods of Metal PBF, the thermal loading period and the stress relaxation period. In the thermal loading period, the layer-by-layer build cycles of Metal PBF are simulated, and the thermal stress accumulated in the build process is predicted. In the stress relaxation period, the removal of parts from the substrate is simulated, and the off-substrate part distortion and residual stress are predicted. Validation of part distortion predicted by the QTM model against both experiment and data in literature showed a relative error less than 20%. This QTM, together with the TCN, offers a framework for rapid, part-scale simulations of Metal PBF that can be used to optimize the build process and parameters.

## 1. Introduction

This manuscript is the second in a two manuscript series (with part 1 found in [1]) describing an algorithm for the fast prediction of thermal distortion in parts printed by the additive manufacturing (AM) process metal powder bed fusion (PBF): also termed direct metal laser sintering, direct metal laser melting, and metal selecting laser melting [2]. Metal PBF uses a layer-by-layer build cycle in which at each layer: 1) a recoater blade spreads a thin layer (20–50 μm) of metal powders at the melt plane; 2) radiant energy is applied to the melt plane by a rastering laser to selectively melt the powder in a two-dimensional (2-D) pattern; and 3) the part is indexed downward to accommodate a new layer of material. As such, three-dimensional (3-D) parts with complex features can be made with relatively low cost in a low-volume production setting (1 – 1000 units [3]); these capabilities are especially attuned to the low-volume, high value-added aerospace and medical industries [3–14].

Thermal distortion is a major challenge in current Metal PBF processes [15–18]. However, this issue may be mitigated with proper selection of the part orientation during the build and the proper design of sacrificial support structures [19–25]. However, proper design is not intuitive, nor well-understood. What is needed is automatic, efficient

* Corresponding author at: Dept. of Aerospace and Mechanical Engineering, University of Notre Dame, United States.
** Corresponding author.
*E-mail addresses:* dgo@nd.edu (D.B. Go), hoelzle.1@osu.edu (D. Hoelzle).
[1] Current affiliation is ITAMCO.

https://doi.org/10.1016/j.addma.2018.05.001
Received 11 October 2017; Received in revised form 26 March 2018; Accepted 1 May 2018
Available online 20 June 2018

algorithms to identify optimal orientations and support designs that minimize part distortion, thermal stress, or any number of objectives. However, to optimize for minimal part distortion, for instance, we must be able to predict thermal distortion and we must make this prediction on the order of one hundred times when using iterative optimization algorithms. Therefore, the prediction must be sufficiently fast to compute an optimal solution in a few hours on a conventional computer, a stated design goal of various United States government entities to expand AM adoption [26–28]. In Part 1 of this two manuscript series [1], we presented a fast thermal model using a Thermal Circuit Network (TCN) to predict the temperature history of a part during a Metal PBF build. In this Part 2, we present the coupling of the TCN output to a quasi-static thermo-mechanical (QTM) model to predict the thermal stress and ultimate part distortion. Collectively, the aim is for these two fast models to form the objective function engine of an optimization strategy for minimizing thermal distortion, thermal stress, or other outputs, of as-built parts.

### 1.1. Select thermo-mechanical models for Metal PBF and Directed Energy Deposition

Comparable models to our TCN/QTM framework have been developed for Metal PBF and the similar technology of Directed Energy Deposition (DED). Here, we provide a cursory overview of a select few thermomechanial models; we have omitted more sophisticated multi-physics models that integrate fluid mechanics and particle migration as there is a mismatch in length scale between these methods and the method presented here. We classify previous attempts by the method of analysis (dynamic or quasi-static) and the size of the simulation domain (Table 1). We define dynamic models as thermomechanical models in which the constitutive equations to the finite element method (FEM) include time derivatives of the state variables. We define quasi-static models as ones in which no time derivative terms are present.

Most existing PBF and DED thermo-mechanical models utilize a dynamic analysis approach, with the exception by Denlinger et al [29], which uses a quasi-static analysis. Although the thermal stress and motion of materials adjacent to the laser spot region is dynamic [12], the thermo-mechanical processes of stress accumulation and part distortion in the entire part behave quasi-statically; the part itself is affixed to a substrate and thus has very low accelerations. It is appealing to forego an accurate, but time-consuming, dynamic analysis for a series of computationally-efficient, quasi-static analyses at time-points of interest.

Additionally, existing models can be classified as either a “meso-scale model” [30–34] or a “part-scale model” [35,36,29,37] based on the size of the simulation domain. The meso-scale models typically predict the evolution of thermal stress and displacement as the laser beam scans across the first or the initial few layers of metal powder. Since the diameter of the laser beam is approximately 100 μm, an extremely fine mesh is required to capture the physics adjacent to the laser spot and these models do not scale well to full part models to understand gross part deformation. On the other hand, part-scale models attempt to simulate thermal distortion and residual stress in considerably larger domain with sizes ranging from 10 mm to 1000 mm. To achieve this goal, laser energy is assumed to be applied to a full layer at once and the influence of scanning patterns is neglected. An exception is the use of the applied plastic strain method [35,38,39] where the thermal strain from a meso-scale model is applied to a part-scale model as successive, strained voxels are added to the part along the laser scan path. The applied plastic strain method allows researchers to study the effect of scan pattern; however, the temperature history of the part is not directly simulated.

Of the existing models, only a small number have reported the computational speed of their algorithms. To the extent to which we are aware, all models require greater than ten hours to compute a thermal distortion solution, making all current models ill-posed for integration into optimization algorithms.

**Table 1**
Representative thermo-mechanical models for Metal PBF and DED.

| Paper | Analysis | Domain (mm) | Speed | Relative Error |
|---|---|---|---|---|
| [30] | Dynamic | 1 × 1 × 1 | / | / |
| [31] | Dynamic | ~4 × 4 × 1 | / | / |
| [32] | Dynamic | 5 × 5 × 4 | / | / |
| [33] | Dynamic | 12.2 × 3.2 × 1.0 | / | / |
| [34] | Dynamic | 20 × 20 × 1 | / | / |
| [35] | Dynamic | ~ 28 × 6 × 6 | / | < 1% |
| [37] | Dynamic | 70 × 15 × 12 | / | / |
| [36] | Quasi-static | 203.2 × 47.6 × 25.4 | / | 4.7%–431% |
| [29] | Quasi-static | 3810 × 457 × 25.4 | 43 h + 71 h | 29% |

### 1.2. Select experimental validations of Metal PBF models

Only a limited number of researchers have clearly reported the accuracy of the distortion prediction in their models. Denlinger et al. [29] conducted a thermo-elasto-plastic analysis for a large, DED printed part by performing a dynamic thermal analysis and a quasi-static incremental analysis. Although a three-stage modeling approach was implemented to reduce the computational time, the thermal and thermo-mechanical model required 43 and 71 h on a 16 core computer, respectively, and the maximum error against experiment in this study was about 29%. Denlinger et al. [36] also developed another model that simulated the self-annealing nature of DED, and reported relative error ranges from 4.7% to 431% with different annealing constants. Keller et al. reported a Metal PBF model based on the applied plastic strain method as discussed above [35]. They reported that the simulated distortion of three cantilever specimens with different laser scanning patterns is almost exactly the same as the measured distortion. Zaeh et al. compared their models to Metal PBF printed cantilevers with different cantilever thickness, layer thickness, and initial platform temperatures [37]. All cantilevers bent downward after being cut off from the support structure, which is resolved by their temperature-dependent model, but would not be resolved by a model that does not leverage temperature information, such as the applied plastic strain method. Wu et al. demonstrated the accurate prediction of the distortion in 316 L stainless steel quadrilateral prisms in horizontal and vertical directions [40]. The $x$, $y$, and $z$ displacements at the prism surfaces were measured by a digital image correlation method, providing some of the most detailed maps of thermal distortion available, and this data set is used as a comparison to our model in Section 5.4.

Thermal stress predictions of printed artifacts have been validated by the destructive crack compliance method, non-destructive X-ray diffraction (XRD), and neutron diffraction analyses. In early studies, Mercelis and Kruth [41] used both a crack compliance method and XRD to measure the thermal stress in samples. They concluded that in general the residual stress profile consists of tensile stress at the top and bottom of the part, and a large zone of intermediate compressive stress in between. Yadroitsava and Yadroitsev [18,42] used XRD to measure residual stress in samples fabricated from steel 316 L and Ti6Al4V alloy. They concluded that (1) thermal stress along the scanning direction is higher than that in the perpendicular directions; (2) maximum stress is found near to the substrate; and (3) thermal stress varies considerably from layer to layer. Recently, Wu and et al. [40] performed parametric studies on the effects of laser scanning pattern, laser power, scanning speed, and build direction on 316 L stainless steel artifacts manufactured by Metal PBF. They concluded that reduction in thermal stress is obtained by decreasing the scan island size, increasing island-to-wall rotation to 45 degrees, and increasing the applied energy per unit length.

### 1.3. Contributions of this work

In this work, we present a fast quasi-static thermo-mechanical (QTM) FEM model for predicting part distortion in Metal PBF and its validation against both our own thermal distortion and stress measurements and data reported by Wu et al. [40]. In our QTM model, at each build cycle a new layer of voxels is added with embedded temperature metadata from our TCN, described in companion manuscript part 1 [1], and this temperature data is used to perform a quasi-static analysis of the induced thermal stress and thermal distortion (Sections 2 and 3). Additionally, the model distinguishes between the Metal PBF build process and the part removal process. In other words, the model can predict part distortion and stress before and after the parts are removed from the substrate. We report our predicted thermal distortion and stress for comparison to measurements on array of test artifacts and data in [40] (Sections 4 and 5). Section 6 presents conclusions and potential future studies.

## 2. Model description

### 2.1. Fundamental mechanical loading mechanism

It may be assumed that Metal PBF is divided into two distinct periods: the thermal loading (TL) period in which the process cycles between thermal expansion and thermal contraction as each layer is applied and the stress relaxation (SR) period in which a single stress relaxation event occurs when the part is removed from the support structure or substrate. Fig. 1(a) demonstrates these periods, and Fig. 1(b) demonstrates the corresponding FEM scheme.

- Thermal Loading (TL)
  - Thermal Expansion (TE):
    Metal powders at the top layer are melted into a melt pool by a laser beam, and lower layers are heated up by conduction from the melt pool and thus expand. The top layer is in a zero-stress state as the layer is in either a powder or liquid phase.
  - Thermal Contraction (TC):
    After the melt pool is fully solidified, the part cools leading to thermal contraction and thus the induction of thermal stress. The top layer is now locked into place and top-layer nodes will now have non-zero stress states.
- Stress Relaxation (SR):
  After the build process is complete, parts are cut off from the substrate and support structures are removed. Due to the release of mechanical constraint, the general node in the part moves to a relaxed stress state, but is distorted from the constrained configuration.

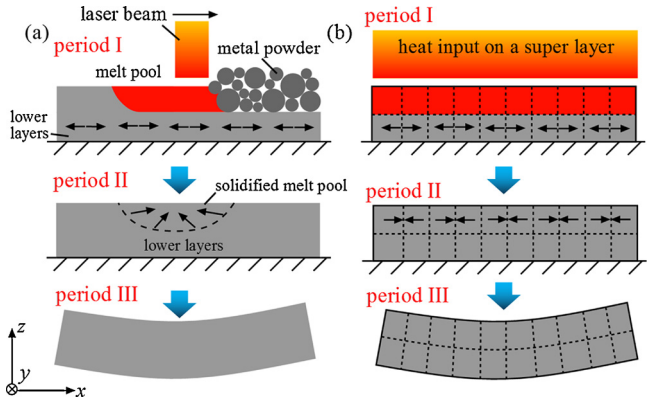


**Fig. 1.** Demonstration of the two distinct periods of the QTM, a cycle of thermal loading (TL) and a stress relaxation (SR) event. (a) Physical process scheme (scheme motivated by [41]) and (b) finite element model (The temperature on each node at each TL cycle is obtained from the TCN model in the companion manuscript, part 1 [1]).

### 2.2. Model assumptions and abstractions

As stated in Section 1, our goal is to simulate the TL and SR periods in a computationally efficient manner. Accordingly, we employ the following assumptions and abstractions to simplify the analysis and reduce computational complexity. The assumption and abstractions match the numbering from the companion manuscript, part 1 [1], where there is overlap.

- *Assumption 1*: The build process is quasi-static and thus inertia effects of materials can be neglected.

*Justification*: Despite the dynamic change of stress and displacement profiles adjacent to the laser spot, the entire part remains approximately static on the substrate during the build process. This practice has been implemented by Denlinger et al [29].

- *Abstraction 1*: Adjacent real build layers with similar temperatures are modeled as one "superlayer", indexed by $i$ ($i = 1, 2, \ldots, I$), and the deposition of one simulated superlayer represents multiple deposition processes of real build layers.
  *Justification*: Modeling a real build layer of ~50 μm has a significant computational cost. However, thermal contraction of the melt pool physically exists in multiple layers as micrographs of Metal PBF printed parts show that the melt pool spans approximately 4–8 real build layers [43]. Others have used superlayers of 0.5 mm [25], 1 mm [37], and 2 mm [44] and demonstrated drastic improvements in computational efficiency with small changes in computed outputs of distortion and residual stress. A more thorough justification of Abstraction 1 and a convergence study comparing superlayer thickness to computed distortion is provided in Appendix A1.
- *Abstraction 2*: The moving heat source from the laser beam scanning across the powder bed is assumed to be a uniform heat input to the topmost superlayer, as shown in Fig. 1(b).
  *Justification*: Because the diameter of the laser beam is about 100 μm, simulating heat transfer at such a small scale prohibits modeling entire parts in a computationally-efficient manner. Furthermore, in the real Metal PBF process, the raster pattern is usually changed at each build cycle (e.g. a default of 67° rotation in an EOS machine), and the influence of this laser scanning pattern is averaged out for a superlayer containing multiple real layers. Motivated by [37,45], scan strategy-dependent process artifacts are assumed to be minimized by good process designs used by industrial PBF tools. A more thorough justification of Abstraction 2 is provided in Appendix A2.

### 2.3. Model Overview

Fig. 2 shows the flow chart of the QTM model which consists of two modules: the TL module and the SR module. Each TL cycle consists of a TC first and then a TE second (Fig. 3). This seemingly reverse order of the TC and TE in a TL is because the powder or liquid phase of the topmost layer during melting is assumed to be in a zero-stress state (Section 2.1). Thermal stress is analyzed as a single quasi-static process driven by the temperature difference at the beginning and end of the TL period. For instance, the time instances at the beginning of each TL period are denoted as $t_1$, $t_2$, $t_3$, … and the temperature of the $i$th superlayer at time instant $t_j$ is denoted as $T_i^{t_j}$ as shown in Fig. 3. The 1st superlayer is cooled down from $T_1^{t_1}$ in the 1st TC period, and then reheated to $T_1^{t_2}$ in the 2nd TE period, which yields a distortion and stress accumulation in the nodes of the 1st layer from the 1st TL period driven by the temperature difference $T_1^{t_2} - T_1^{t_1}$. The TC period comes after the preceding TE period and lasts until the beginning of the next TE period

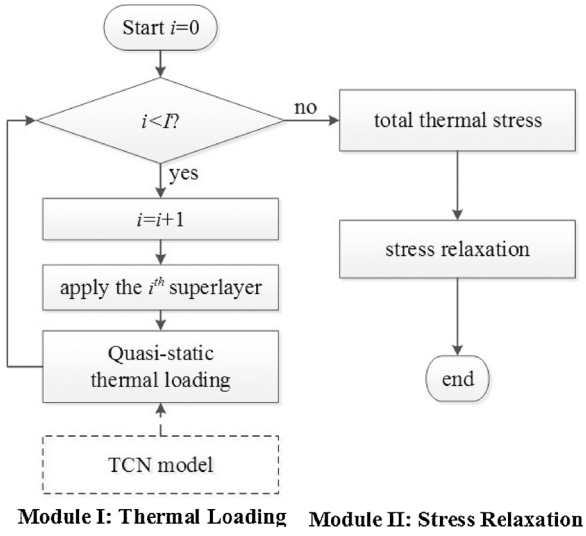


**Fig. 2. Simulation flow chart of the quasi-static thermo-mechanical model.** The simulation runs through Module I: Thermal Loading until the total number of superlayers $I$ are analyzed, at which point it conducts the final analysis in Module II: Stress Relaxation.

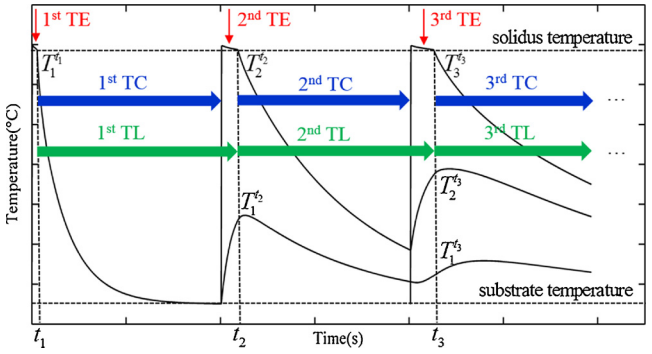


**Fig. 3. Description of the TL module.** Each TL period consists of a TE and TC process as indicated by the temperature history of each superlayer. The temperature history is imported from the TCN detailed in manuscript part 1.

(or the end of the build process for the last superlayer), as shown by the blue arrows in Fig. 3. During TC periods, all fused superlayers cool down for a given period of time, which is termed the inter-layer dwell time.The temperature history of the part – each $T_{(\cdot)}^{(\cdot)}$ variable – is predicted by a TCN model from the companion paper [1] (TCN Model block from Fig. 2). In brief, parts are discretized into thermal nodes by approximating the relative amount of vertical and horizontal heat transfer in a given superlayer, and then principles from heat transfer and conservation of energy are applied to each superlayer during the Metal PBF build, producing a temperature history for each superlayer. Part 1 [1] details the model, its underlying assumptions and abstractions, and validation against FEM thermal analysis.

After the Metal PBF process is complete, parts are physically removed from the substrate and there is a stress relaxation process, which we simulate with the SR module. Driven by the thermal stress accumulated in the TL period, the removal of the mechanical constraint will generally yield a reduction in the stress and increase in distortion. The SR period is a non-typical structural mechanics problem because the initial stress in the part is nonzero. Additionally, the boundary condition is a free boundary condition, which causes a singularity problem as will be discussed in detail in Section 3.3.

### 2.4. Part and support material properties

The part and support structures in the QTM model are represented by rectangular cuboidal voxels [46,47]. Fig. 4(a) and (b) show the voxel representation of a horizontal disk and a disk at an angle of 35° to the substrate together with their support structures. Each voxel is categorized either as a *part voxel* or a *support voxel*. Fig. 4(c) shows a voxel used as a rectangular cuboidal element in FEM analysis.

The mechanical properties of Young's modulus, $E$, and yield stress, $\sigma^Y$, vary with temperature. We use established mechanical property versus temperature relationships and linearly interpolate the properties using the average of the initial and final temperature of a node for a given TL period as the interpolation point. Physical properties of density and thermal expansion coefficient, $\alpha$, are assumed to not be temperature varying.

Support structures are usually lattice structures generated underneath overhanging surfaces with inclination angles less than 35° to the substrate [20,22,24,48]. The mechanical properties of support structures are complex functions of the bulk material properties, topology of the lattice structure, and volume fraction of solid in the support structure. Similar to other works in Metal PBF [49,50], we leverage the simple Gibson-Ashby theory for cellular solids in this study [51] to modify the effective material and physical properties of the supports

$$\alpha_s = \alpha;\ E_s = E\phi_s^2;\ \sigma_s^Y = \phi_s\sigma^Y, \tag{1}$$

where $\phi_s$ is the volume fraction of the support.

## 3. Numerical implementation

### 3.1. Basic laws and FEM formulation

Because the thermo-mechanics of Metal PBF build process are modeled using the quasi-static assumption, Assumption 1, the governing equation in the simulation domain $\Omega$ is

$$\nabla\cdot\boldsymbol{\sigma} = 0 \text{ in } \Omega, \tag{2a}$$

where $\boldsymbol{\sigma}$ is the stress tensor. $\Gamma$ is the entire part boundary, which is composed of sub-boundaries $\Gamma_{\mathbf{u}}$, the boundary in contact with the substrate, and $\Gamma_{\mathbf{t}}$, the free boundary. J2 plasticity theory [52] is applied with the following assumptions:

- *Assumption* 2: The parts are geometrically linear.
  *Justification*: The parts in Metal PBF are usually not highly flexible structures [53] and geometric nonlinearity is negligible.
- *Assumption* 3: The associative flow rule is used.
  *Justification*: Experiments show that the associative flow rule is accurate for metal materials [52].

Thus, the stress tensor $\boldsymbol{\sigma}$ is related to strain by

$$\boldsymbol{\sigma} = \mathbf{C}\boldsymbol{\varepsilon}_e;\ \boldsymbol{\varepsilon} = \boldsymbol{\varepsilon}_e + \boldsymbol{\varepsilon}_p + \boldsymbol{\varepsilon}_T, \tag{2b}$$

where $\mathbf{C}$ is the fourth-order material stiffness tensor, and $\boldsymbol{\varepsilon}_e$, $\boldsymbol{\varepsilon}_p$, and $\boldsymbol{\varepsilon}_T$ are the elastic, plastic, and thermal strain tensors, respectively. The thermal strain tensor is defined as

$$\boldsymbol{\varepsilon}_T = \begin{bmatrix} \alpha(T-T_r) & 0 & 0 \\ 0 & \alpha(T-T_r) & 0 \\ 0 & 0 & \alpha(T-T_r) \end{bmatrix}, \tag{2c}$$

where $\alpha$ is the thermal expansion coefficient and $T_r$ is the room temperature.

The plastic strain $\boldsymbol{\varepsilon}_p$ is computed with the return mapping algorithm [54] by applying the von Mises yield function with both isotropic and kinematic hardening effects [55]

$$f(\boldsymbol{\eta}, e_p) = \|\boldsymbol{\eta}\| - \sqrt{2/3}\,[\sigma_y^0 + (1-\beta)He_p] \le 0, \tag{3a}$$

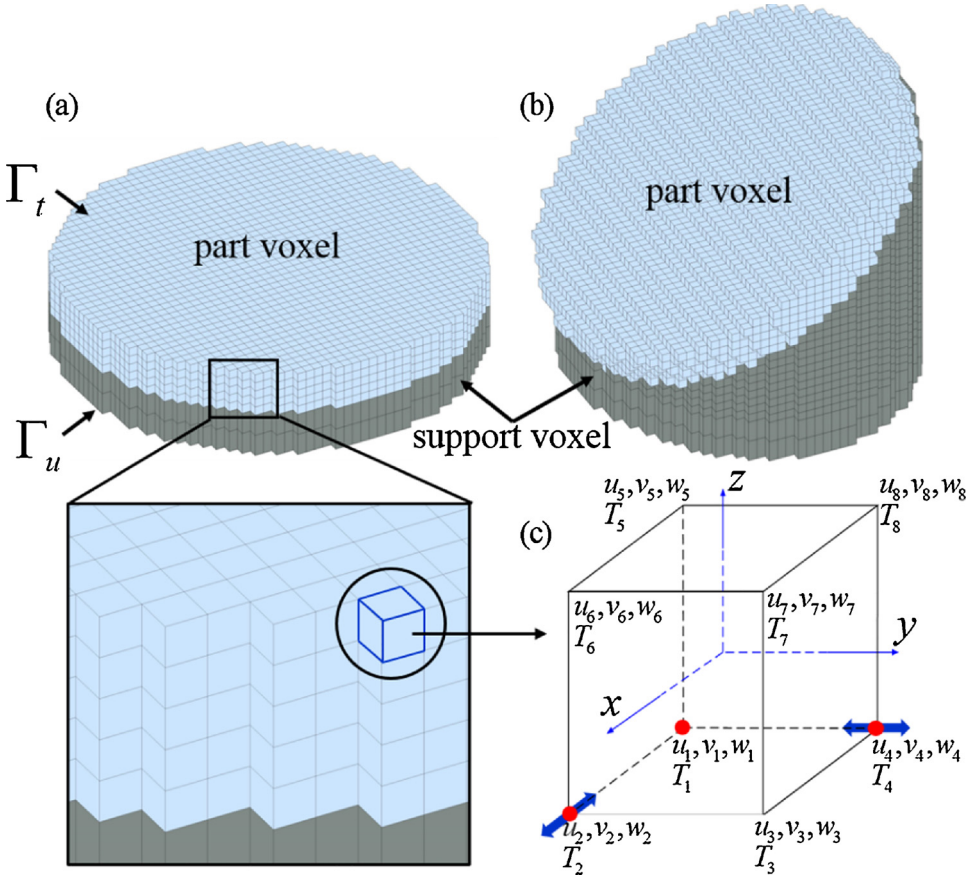


**Fig. 4. Rectangular cuboidal voxel representation of disk artifacts for FEM analysis.** (a) Horizontal orientation and (b) oriented 35° to the substrate. (c) A voxel used as a rectangular cuboidal element in FEM analysis. The red dot and the blue arrow denote the boundary condition applied during the SR module.

and the associative flow rule, defined by

$$\dot{\varepsilon}_p = \dot{\gamma}\frac{\partial f(\boldsymbol{\eta}, e_p)}{\partial \boldsymbol{\eta}} = \dot{\gamma}\mathbf{N}. \tag{3b}$$

Here, $\gamma$ is the plastic consistency parameter, $\mathbf{N}$ is the unit deviatoric tensor normal to the yield surface, $H$ is the plastic modulus, $\sigma_y^0$ is the original yield stress, and $\beta$ is a parameter to account for the combined hardening effect ($\beta = 0$ stands for pure isotropic hardening, $\beta = 1$ stands for pure kinematic hardening, and $0 < \beta < 1$ stands for combined hardening). The bracket $\|\|$ is the magnitude operator to a tensor. The effective plastic strain $e_p$ is defined as

$$e_p = \sqrt{\frac{2}{3}\boldsymbol{\varepsilon}_p : \boldsymbol{\varepsilon}_p}, \tag{3c}$$

where : is the double dot product operator on two tensors. The shifted stress tensor $\boldsymbol{\eta}$ is defined as

$$\boldsymbol{\eta} = \mathbf{s} - \boldsymbol{\sigma}_{\text{back}}, \tag{3d}$$

where $\mathbf{s}$ is the deviatoric stress tensor and $\boldsymbol{\sigma}_{\text{back}}$ is the back stress which is proportional to the plastic strain

$$\dot{\boldsymbol{\sigma}}_{\text{back}} = \frac{2}{3}\beta H\dot{\gamma}\mathbf{N}. \tag{3e}$$

The following shows the FEM formulation for a rectangular cuboidal element as shown in Fig. 4(c). Each node of the rectangular cuboidal element has four degrees of freedom (DOF): temperature $T$ and $x$, $y$, and $z$ displacements denoted as $u$, $v$, and $w$, respectively. The temperature $T$ is imported from the TCN model presented in the companion manuscript [1]. If temperature and displacement at node $j$ are denoted by $T_j$, $u_j$, $v_j$, $w_j$, the temperature and displacement within the rectangular cuboidal element are

$$T = \{N\}^T\{T\} = \{T\}^T\{N\}; \tag{4a}$$

$$\mathbf{u} = \begin{Bmatrix} u \\ v \\ w \end{Bmatrix} = \begin{Bmatrix} \{N\}^T\{u\} \\ \{N\}^T\{v\} \\ \{N\}^T\{w\} \end{Bmatrix} = [\hat{N}]\{d\}, \tag{4b}$$

where $\{T\} = \{T_1 \;\; T_2 \;\; \cdots \;\; T_8\}^T$, $\{u\} = \{u_1 \;\; u_2 \;\; \cdots \;\; u_8\}^T$, $\{v\} = \{v_1 \;\; v_2 \;\; \cdots \;\; v_8\}^T$, $\{w\} = \{w_1 \;\; w_2 \;\; \cdots \;\; w_8\}^T$, $\{N\}$ is the shape function,

$$\{d\} = \{u_1 \;\; v_1 \;\; w_1 \;\; \cdots \;\; u_8 \;\; v_8 \;\; w_8\}^T, \tag{4c}$$

and $[\hat{N}]$ can be derived from $\{N\}$. The incremental FEM equation can be developed from Eq. (2a) as [55]

$$[K_e^{\tan}]\{\delta d\} = \{F_e^{\text{ext}}\} - \{F_e^{\text{int}}\}, \tag{5a}$$

where $[K_e^{\tan}]$, $\{F_e^{\text{ext}}\}$ and $\{F_e^{\text{int}}\}$ represent the tangent stiffness matrix, external force vector and internal force vector, respectively, and are defined as

$$[K_e^{\tan}] = \int [B]^T[Z^{\tan}][B]dV; \tag{5b}$$

$$\{F_e^{ext}\} = \int [B]^T[Z^{\tan}]\{\varepsilon_T\}dV; \tag{5c}$$

$$\{F_e^{\text{int}}\} = \int [B]^T\{\sigma\}dV. \tag{5d}$$

The term $[B]$ can be derived from the gradient of $[\hat{N}]$, $[Z^{\tan}]$ is the tangent modulus matrix determined by the stress state [55], and finally $\{\sigma\}$ and $\{\varepsilon_T\}$ are stress and thermal strain in Voigt notation

$$\{\sigma\} = \{\sigma_{xx} \;\; \sigma_{yy} \;\; \sigma_{zz} \;\; \sigma_{yz} \;\; \sigma_{xz} \;\; \sigma_{xy}\}^T \tag{5e}$$

$$\{\varepsilon_T\} = \{\alpha(T - T_r) \;\; \alpha(T - T_r) \;\; \alpha(T - T_r) \;\; 0 \;\; 0 \;\; 0\}^T \tag{5f}$$

The governing equation of an element as shown in Eq (5a) is then

used to build the global governing equations for the TL and SR periods.

### 3.2. Modeling TL periods

In the thermal loading (TL) periods, the bottom of the part (or support structures) are fixed on the substrate and other surfaces are free to move. Thus, the boundary and initial conditions are

$$\mathbf{u}(\mathbf{x}, t) = 0 \quad \text{on} \quad \mathbf{x} \in \Gamma_{\mathbf{u}} \tag{6a}$$

$$\mathbf{t}(\mathbf{x}, t) = 0 \quad \text{on} \quad \mathbf{x} \in \Gamma_{\mathbf{t}} \tag{6b}$$

$$\mathbf{u}(\mathbf{x}, 0) = 0 \quad \text{on} \quad \mathbf{x} \in \Omega \cup \Gamma \tag{6c}$$

$$\boldsymbol{\sigma}(\mathbf{x}, 0) = 0 \quad \text{on} \quad \mathbf{x} \in \Omega \cup \Gamma \tag{6d}$$

where $\mathbf{u}$ is the displacement, $\mathbf{t}$ is the surface traction, $\boldsymbol{\sigma}$ is the stress, $\Gamma_{\mathbf{u}}$ represents a boundary in contact with the substrate, $\Gamma_{\mathbf{t}}$ represents the free boundary, $\Omega$ and $\Gamma$ are the simulation domain and its boundary.

At the beginning of each TL period, new rectangular cuboidal elements are added to the FEM model, representing the addition of a new superlayer. The governing equation for all deposited superlayers is the analog of Eq. (5a).

$$[K^{\tan}]\{\delta D\} = \{F^{\text{ext}}\} - \{F^{\text{int}}\} \tag{7}$$

where $\{D\}$ is the nodal displacement of all deposited rectangular cuboidal elements, and global matrices $[K^{\tan}]$, $\{F^{\text{ext}}\}$, and $\{F^{\text{int}}\}$ are obtained by assembling the elemental matrices shown in Eqs. (5b), (5c), and (5d). As more superlayers are deposited, the size of the matrices in Eq. (7) continue to increase until the end of the build. Eq (7) is solved by a modified version of the Newton-Raphson (NR) method using the incremental force method with an adaptive loading step [55] to increase the solver's stability and convergence speed. NR is iteratively solved until the norm of the right-hand side (RHS) of Eq. (7) is less than $10^{-6}$ N.

### 3.3. Modeling the SR period

In the SR period, the part is removed from the substrate and support structures are removed. The boundary and initial conditions for the SR period are

$$\mathbf{t}(\mathbf{x}, t) = 0 \quad \text{on} \quad \mathbf{x} \in \Gamma \tag{8a}$$

$$\mathbf{u}(\mathbf{x}, 0) = \mathbf{u}_{\text{TL}} \quad \text{on} \quad \mathbf{x} \in \Omega \cup \Gamma \tag{8b}$$

$$\boldsymbol{\sigma}(\mathbf{x}, 0) = \boldsymbol{\sigma}_{\text{TL}} \quad \text{on} \quad \mathbf{x} \in \Omega \cup \Gamma \tag{8c}$$

where $\mathbf{u}$ is the displacement, $\mathbf{t}$ is the surface traction, $\boldsymbol{\sigma}$ is the stress, $\mathbf{u}_{\text{TL}}$ and $\boldsymbol{\sigma}_{\text{TL}}$ are the total displacement and stress accumulated in the TL periods, and $\Gamma$ is the boundary of the entire part domain Ω. It should be noted that strictly enforcing the boundary condition in Eq. (8a) will cause a singularity problem because the part is free to move and there are an infinite number of solutions to the problem. To avoid this singularity while still allowing the part to distort freely during the SR period, the boundary condition illustrated in Fig. 4(c) is used to constrain translation of a single node and rotation of two adjacent nodes, while allowing free motion of all other nodes. First, three nodes (node 1, 2, and 4) of an arbitrary rectangular cuboidal element are located as shown in Fig. 4(c). Node 1 is fixed along $x$, $y$ and $z$. Node 2 is fixed along $y$ and $z$ but allowed to move freely along the $x$ direction. Node 4 is fixed along $x$ and $z$ but allowed to move freely along the $y$ direction.

The governing equation for the SR period is

$$[K^{\tan}]\{\delta D\} = -\{F^{\text{int}}\}, \tag{9a}$$

where $\{D\}$ is the nodal displacement of all rectangular cuboidal elements, and $[K^{\tan}]$ and $\{F^{\text{int}}\}$ are global tangent stiffness and internal force matrices, which are obtained by assembling $[K_e^{\tan}]$ in Eq. (5b) and $\{F_e^{\text{int}}\}$ in Eq. (5d) for all rectangular cuboidal elements. At the beginning of the first NR iteration, the residual stress is the accumulated stress at the completion of TL periods, and we have

$$\{F_e^{\text{int}}\} = \int [B]^T \{\sigma_{\text{TL}}\} dV, \tag{9b}$$

where $\{\sigma_{\text{TL}}\}$ is the Voigt notation of $\boldsymbol{\sigma}_{\text{TL}}$. Again, NR with adaptive loading is applied until the norm of the RHS of Eq. (9a) is less than $10^{-6}$ N.

## 4. Model validation methods

This section details an array of direct and quantitative comparisons between the TCN-QTM model (combining manuscripts parts 1 and 2) and printed artifacts. The first validation set is an array of 316 L stainless steel and AlSi10Mg artifacts printed by the authors in the form of simple disks of varying dimensions. Top surface distortion and von Mises stress are characterized by a coordinate measuring machine and neutron diffraction. We also compare the TCN-QTM model to the detailed distortion and stress quantifications of pyramid structures printed in 316 L stainless steel [40].

### 4.1. Disk artifact printing

Disk samples were built from AlSi10Mg and 316 L stainless steel powder feedstock with EOS M290® Metal PBF machines at two different locations (AlSi10Mg at the University of Pittsburgh and 316 L at the Johnson & Johnson Company). The EOS M290® has a build volume of 250 × 250 × 325 mm and a Yb-fiber laser with spot size of 100 µm. Default EOS settings were used for all builds. The power and scanning speed of the laser beam were set to 280 W and 2.0 m/s for AlSi10Mg and 195 W and 1.083 m/s for 316 L stainless steel. The substrate temperature was set to 35 °C for AlSi10Mg and 80 °C for 316 L stainless steel. The powder layer thickness was set to 30 µm for AlSi10Mg and 20 µm for 316 L stainless steel. An alternating scan pattern was applied, where the scan direction was rotated by 67° between consecutive layers. The entire build process was maintained in an ultra-high purity argon gas and the oxygen content less than 0.1%.

Disk artifacts were printed with different materials, dimensions and orientations to test a range of material characteristics and geometries to validate our model over a wide design space (Case Nos. 1–14 in Table 2 and Fig. 5). Case Nos. 1–3 have the same disk geometry, but have different perturbations to the manufacturing process. To first quantify a variable not captured by our model, we studied the influence of build plate location and proximity to other artifacts by printing two sets of identically-printed, clustered disks (denoted clusters 1 and 2), and six (AlSi10Mg) / four (316 L) disks printed individually in the center of the build plate (Case Nos. 1 and 2 shown in Fig. 5(a)). Angled disks were

**Table 2**
Catalog of disk artifacts printed.

| Case No. | Artifact Description | No. of samples | Material | Diameter (mm) | Thickness (mm) | Angle (degree) |
|---|---|---|---|---|---|---|
| 1 | Clustered and centered disks | 36 | AlSi10Mg | 45 | 5 | 0 |
| 2 | | 34 | 316 L | | | |
| 3 | Angled disks | 2 | 316 L | 45 | 5 | 35 |
| 4 | Disks with different diameters | 1 | AlSi10Mg | 55 | 5 | 0 |
| 5 | | 1 | | 65 | | |
| 6 | | 1 | | 70 | | |
| 7 | | 1 | | 75 | | |
| 8 | Disks with different thicknesses | 2 | AlSi10Mg | 45 | 1 | 0 |
| 9 | | 2 | | | 2 | |
| 10 | | 2 | | | 3 | |
| 11 | | 2 | | | 10 | |
| 12 | | 2 | | | 15 | |
| 13 | | 2 | | | 20 | |
| 14 | | 2 | | | 30 | |

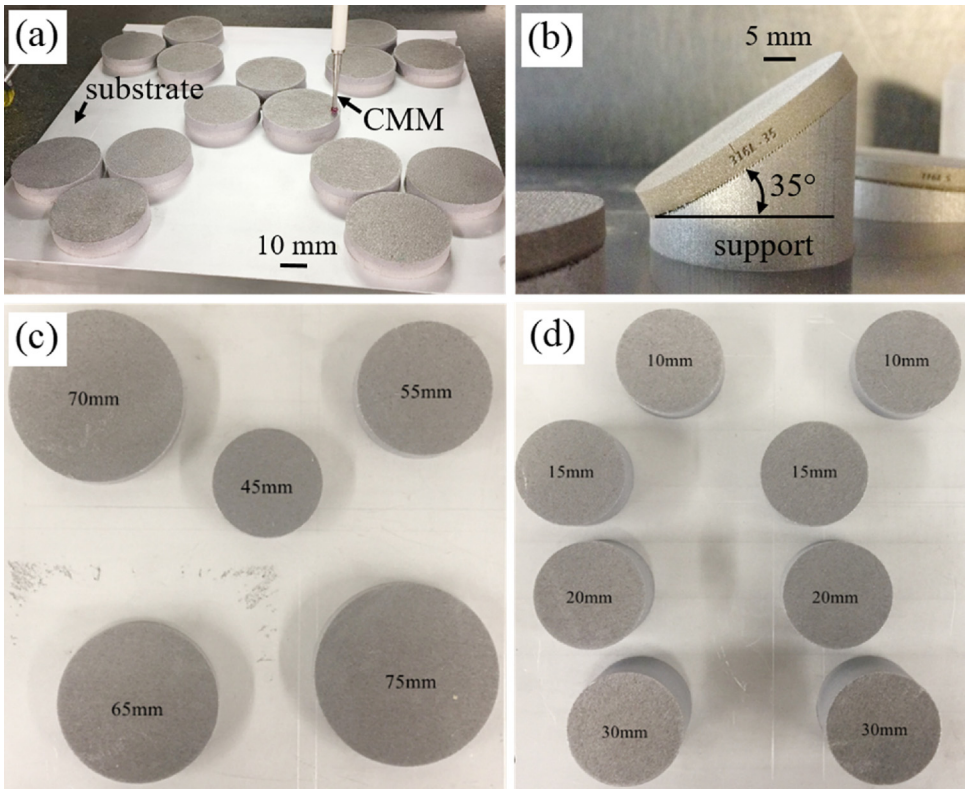


**Fig. 5.** Experimental samples: (a) Horizontal clustered disks with 45 mm diameter and 5 mm thickness built at different locations of the substrate (note the probe of the coordinate measuring machine (CMM)); (b) disks with diameter 45 mm and thickness 5 mm built and an inclination of 35° to the substrate; (c) disks with thickness 5 mm and diameters 45, 55, 65, 70 and 75 mm; and (d) disks with 45 mm diameter and thickness 10, 15, 20 and 30 mm.

printed to test the model for a design in which the axis of symmetry of the part is not aligned with the machine $z$-direction during the build (Fig. 4(b) and Fig. 5(b)). Lastly, disks with different diameters (Fig. 5(c), Case Nos. 4–7) and different thicknesses (Fig. 5(d), Case Nos. 8–14) tested our model with different disk geometries. A fragmented grid support design with a tooth interface with the part was used. By measuring a piece of support structure, we found the supports have design parameters of a rectangular grid with 0.78 mm center-to-center spacing, 0.19 mm wall thickness and a tooth interface with the part. Support volume fraction, $\phi_s$, is calculated to be 0.42. Different support removal procedures were used, depending on the purpose. 316 L Material. Case 3 and the subset of Case 2 that was dedicated to radius of curvature (ROC) measurements used the standard protocol of industry partner Johnson & Johnson: a bandsaw was used to separate the support from the substrate and then the support was removed from the part by chisel and bead blast. For the subset of Case 2 dedicated to residual stress measurement, neutron diffraction measurements were taken when the disks were still on the substrate. AlSi10Mg Material. The ROC measurements for the 316 L disks did not display an appreciable difference between the removed from substrate case and the support removed case (data not shown); the supports use a fragmented grid pattern, providing a negligible increase in the bending stiffness. Accordingly, AlSi10Mg samples were simply removed from the substrate by bandsaw and the support structure was left on.

### 4.2. Disk artifact characterization

The topography of the top surface of each disk artifact was measured using a general purpose Renishaw® Cyclone Series 2 coordinate measuring machine (CMM) with a Renishaw®'s SP620 touch trigger probe with a 3 mm tip diameter both before and after the artifacts were removed from the substrate. The CMM has a 1 μm position resolution with axial repeatability of ± 2 μm. Each measurement was repeated three times with a different datum location at each repeat.

When built horizontally, a disk artifact bends into a "bowl" shape. The top surface is curve fitted to a sphere using a least squares approach, and the distortion of the disk is quantified by the radius of curvature (ROC) of the curve fit sphere. When built at an angle to the substrate, the disk typically bends upward with large distortion along the major direction and small distortion perpendicular to that direction, forming an "ellipsoidal bowl" shape. In such a case, the top surface is curve fitted to a torus, and the distortion of the disk is quantified by the ROC along the major direction.

Neutron diffraction residual stress measurements were performed on the L3 diffractometer of the Canadian Neutron Beam Centre, located in the NRU reactor, at Canadian Nuclear Laboratories. Neutrons with wavelength of 1.508 Å diffracted from the {511} planes of a germanium monochromator were employed. The incident beam cross-section was set using 2 mm × 2 mm apertures. The residual stresses within the disk were measured when it was attached to the build plate and support structures. Measurements were performed at a series of locations along longitudinal ($x$) and transverse ($y$) directions at three different heights ($z_1$, $z_2$, $z_3$). More detail on the stress measurement methods can be found in our recent publication [56].

### 4.3. Experiment by Wu et al

To diversify the validation set, we compared our TCN-QTM model to experimentally measured distortion and residual stress in 316 L stainless steel quadrilateral prisms built with a Concept Laser M2® conducted by Wu et al. [40]. The prisms were built in both the horizontal and vertical directions and had a base length of 50 mm, height of 60 mm, and thickness of 10 mm. Wu used digital image correlation (DIC) to characterize the displacement field of the surfaces after removal from the build platform by electrical discharge machining. Residual stress was measured by neutron diffraction.

### 4.4. TCN-QTM model parameters

The TCN-QTM model is run to compare against the experimental artifacts here and in Wu et al. [40]. The TCN-QTM models uses the exact same. stl file as used in the disk experiments and we created our

own. stl file to match the geometry reported in Wu et al. [40]. The effective inter-layer dwell time is estimated by running a small simulation experiment at mid-height of the part with the real layer thickness and real inter-layer dwell time (50 µm and 10 s here). The effective inter-layer dwell time is adjusted to such that the thermal decay rates match. According to the experimental setup, support structures with a thickness 5 mm and a volume fraction of 42% are simulated by 2 superlayers before the deposition of any part material. The substrate temperature is set to 35 °C for AlSi10Mg and 80 °C for 316 L stainless steel and the room temperature is set to be 20 °C to match the physical values applied during disk printing (Section 4.1). The voxel size for all horizontal disks (Case Nos. 1–2 and 4–14) is 3 × 3 mm along $x$ and $y$, and 1 mm along $z$. The voxel size for the disks printed at a 35° angle orientation to substrate (Case No. 2) and the prism samples is 2 × 2 × 2 mm. In all simulations, each single layer of voxels represents a superlayer. The bulk material properties for AlSi10Mg and 316 L stainless steel are given in Appendix A3.

## 5. Results and discussion

### 5.1. Case Nos. 1 and 2. Clustered and centered horizontal disks

Fig. 6 shows contours of the TCN-QTM modeled on-substrate and off-substrate z-direction displacement, $\mathbf{u}_w$, and stress, $\boldsymbol{\sigma}$, for the AlSi101Mg horizontal disk with diameter 45 mm and thickness 5 mm. When the disk is on the substrate, the disk is rigidly constrained to the substrate and thus the displacement of the disk is relatively small with the $z$-displacement generally less than 0.1 mm (Fig. 6(a)); due to thermal contraction, the $z$-displacement is mostly negative, except at the edge of the disk where the edge pulls up due to the integration of stress throughout the part. After the removal of the mechanical constraint in the SR phase, the "bowl" shape is even more distinct (Fig. 6(b)), yielding a maximal edge to center displacement of approximately 0.28 mm. Likewise, these trends hold for the 316 L TCN-QTM model (data not shown).

The on-substrate von Mises stress in the disk is shown in Fig. 6(c). The stress distribution is approximately uniform with the stress at the center slightly larger than those near to the edge. The stress distribution is approximately uniform because the von Mises stress exceeds the yield stress throughout the majority of the material, relaxing to the yield stress as modeled by the return mapping algorithm (Section 3.1). The von Mises stress after the SR phase is shown in Fig. 6(d); the stress is considerably reduced due to the release of the constraint (Section 3.3) imposed by the fixed substrate.

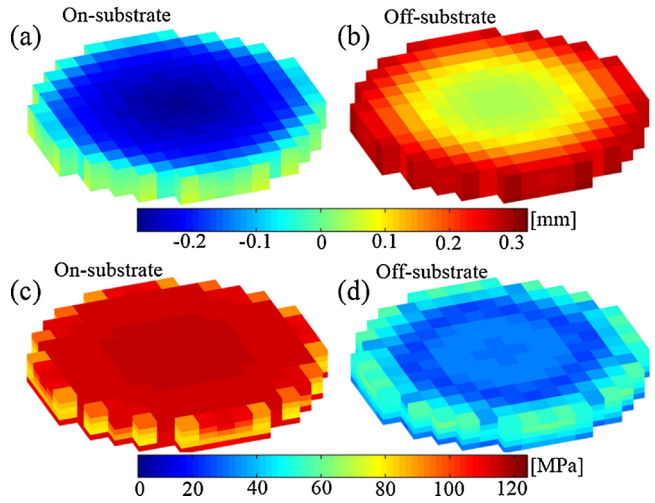


**Fig. 6. Case Nos. 1 and 2: Representative TCN-QTM model results for a horizontally-built AlSi10Mg disk with diameter 45 mm and thickness 5 mm.** (a) and (b) On-substrate and off-substrate $z$-displacement, $\mathbf{u}_w$, in the disk. (c) and (d) On-substrate and off-substrate von Mises stress in the disk.

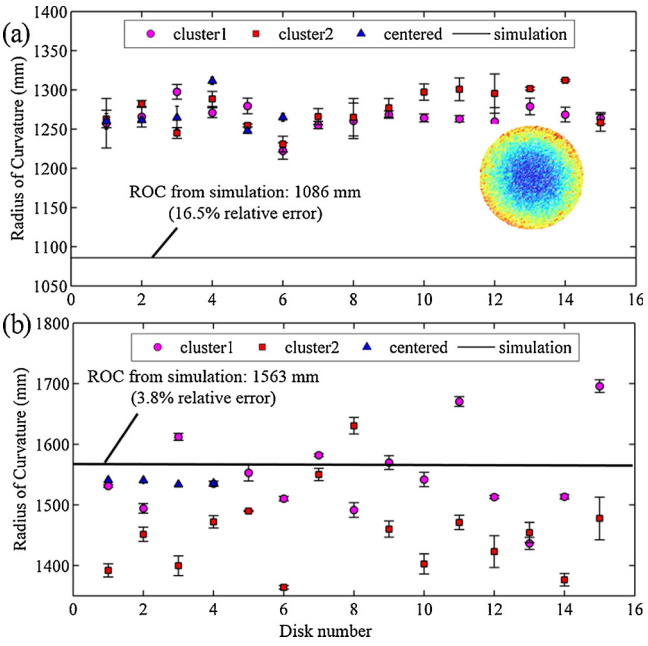


**Fig. 7. Case Nos. 1 and 2: Experimental and TCN-QTM model ROC of horizontally-built disks with diameter 45 mm and thickness 5 mm.** Representative CMM scan inset demonstrates an approximately radially symmetric displacement contour. (a) AlSi10Mg disks and (b) 316 L stainless steel disks.

The experimental ROCs of the horizontal clustered and centered disks are shown in Fig. 7 for both (a) AlSi10Mg and (b) 316 L stainless steel, along with the simulated ROC. The ROC values of cluster 1 and cluster 2 were relatively consistent, indicating the repeatability of both the Metal PBF process and CMM measurements. For centered AlSi10Mg disks, the ROC ranged from 1247.77 ± 0.40 mm to 1311.63 ± 4.67 mm. The ROC of the AlSi10Mg disk clusters was either within or close to this range, indicating that build location had little effect on part distortion. Similar conclusions can be reached for the 316 L stainless steel disks. For both materials, the simulated ROC had average relative errors of 16.5% (AlSi10Mg) and 3.8% (316 L stainless steel), respectively, when compared to the measured data. Interestingly, for AlSi10Mg, the model over-predicted the actual distortion whereas for 316 L stainless steel, the model under-predicted the actual distortion.

Fig. 8 shows the comparison between the experimental and simulated on-substrate stress ($\sigma_{xx}$, $\sigma_{yy}$ and $\sigma_{zz}$) along the diameter of the 316 L stainless steel disk at different $z$-heights (1.25, 2.5 and 3.75 mm from the disk bottom). The simulated results qualitatively match the experimental results, both showing relatively high $\sigma_{xx}$ and $\sigma_{yy}$, and relatively low $\sigma_{zz}$ at all three $z$-height levels. In addition, both experiment and simulation show compressive stresses $\sigma_{xx}$ and $\sigma_{yy}$ near the bottom of the disk (1.25 mm) and high tensional stresses $\sigma_{xx}$ and $\sigma_{yy}$ at the middle and top level of the disk (2.5 and 3.75 mm). The simulated distribution of $\sigma_{xx}$ and $\sigma_{yy}$ at the middle and top level of the disk match the general trend of the experimental results with higher stress at the center of the disk ($y$ = 22.5 mm) and lower stress at the edge.

### 5.2. Case No. 3. Angled disk

For the angled disk, the predicted out-of-plane distortion of the top surface by the TCN-QTM model both qualitatively and quantitatively matches the measured top surface (Fig. 9). Both show larger displacement along the inclination direction (major direction). The ROC along

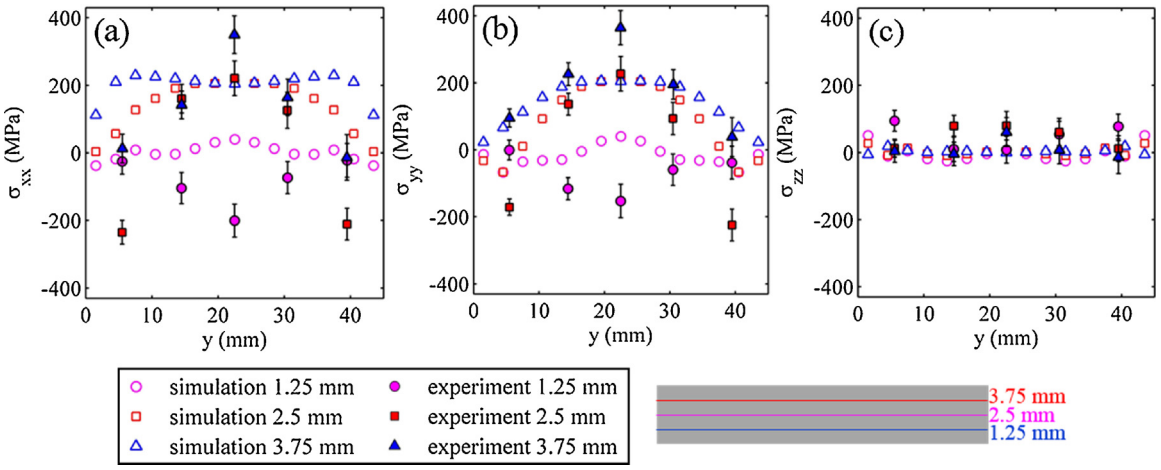


**Fig. 8. On-substrate stress along the diameter and at different z-heights of the 316 L stainless steel disk with diameter 45 mm and thickness 5 mm.** (a) $\sigma_{xx}$, (b) $\sigma_{yy}$, and (c) $\sigma_{zz}$.

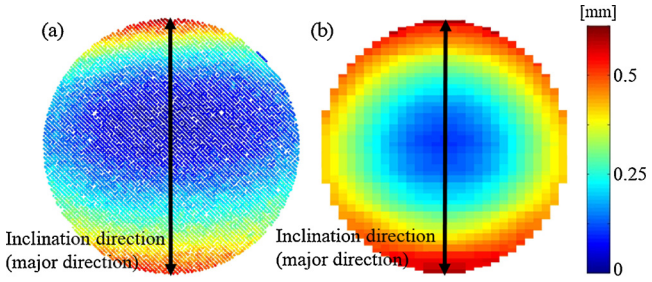


**Fig. 9. Off-substrate out-of-plane displacement of a disk built 35° to the horizontal.** Out-of-plane displacement is the component of **u** in the direction normal to the disk face. (a) experiment and (b) simulation.

the major direction was 410 mm in the experiment and 335 mm in the simulation; a difference of 18.3% and similar to that observed in the horizontal builds. In comparison to disks built with a horizontal orientation, the distortion of the angled disk was greater, with the ROC decreasing from 1086 mm to 335 mm. In the direction perpendicular to the inclination direction, our TCN-QTM model over-predicts the distortion.

### 5.3. Case Nos. 4–14: disks with different diameters and thicknesses

A comparison between the TCN-QTM modeled and experimental ROCs of disks with different diameters and thicknesses is shown in Fig. 10. For disks with thickness 5 mm and diameter 45, 55, 65, 70, and 75 mm, the relative errors in the ROC between the simulations and experiment are 16.5%, 8.1%, 0.7%, 3.9%, and 9.4%, respectively. Similarly, for disks with diameter 45 mm and thicknesses of 5 and 10 mm, the relative error between simulation and experiment were 14.4% and 9.0%. However, for thin disks with thickness 1, 2 and 3 mm, the difference between simulation and experiment is much larger. This is because when disks are thin, the distorted shape of the top surface is no longer a “bowl” shape due to buckling, as shown by the inset in Fig. 10(b); thin disk buckling is either an artifact of the support removal process or perhaps a phenomenon not captured by our model indicating that the TCN-QTM model may not be appropriate for thin-walled structures. Lastly, the distortion of printed disks with thickness 15, 20, and 30 mm was so small that it could not be fit to a sphere. Likewise, the TCN-QTM models predicts large ROCs of 2211, 3142 and 4651 mm, respectively.

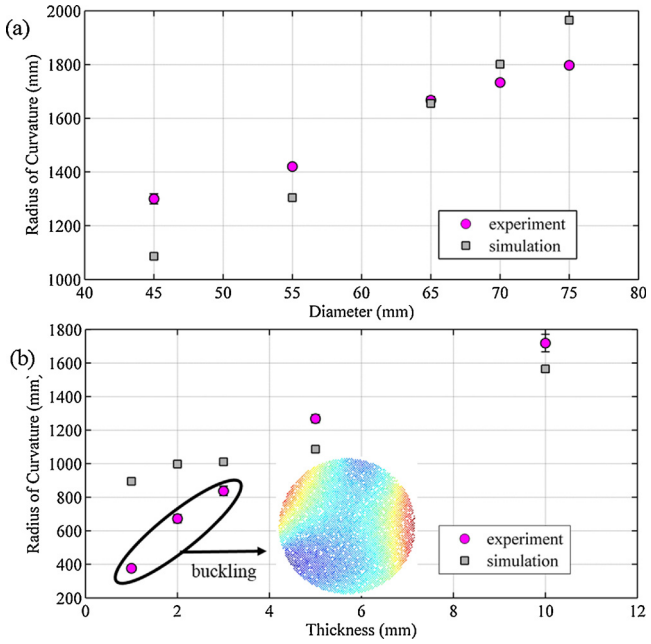


**Fig. 10. ROC of horizontally-built AlSi10Mg disks with various diameters and thicknesses.** (a) ROC of disks with thickness 5 mm and diameter 45, 55, 65, 70 and 75 mm and (b) ROC of disks with diameter 45 mm and thickness 1, 2, 3, 5 and 10 mm.

### 5.4. Comparison to quadrilateral prisms built by Wu et al

Fig. 11 through Fig. 13 show the comparison of the experimental results by Wu et al. [40] and the simulation results by our TCN-QTM model. In general, although we ignored the details of laser scanning patterns studied by Wu et al., the displacements from our simulations both qualitatively and quantitatively matched the experimental results. The prism built in horizontal showed a spherical distortion, with three corners bending away from the substrate (Fig. 11). The displacements along *x* and *y* were induced by shrinkage after the prism is removed from substrate. The prisms built in vertical direction also showed a spherical distortion shape with the two bottom corners of the prism bending away from the substrate (Fig. 12). The negative *z* displacement at the bottom of the prism is due to Poisson’s effect.

Fig. 13(a–c) show the off-substrate stress contour in the vertically-built prism predicted by the TCN-QTM model compared to the data from Wu et al. There is a qualitative match between the experimental

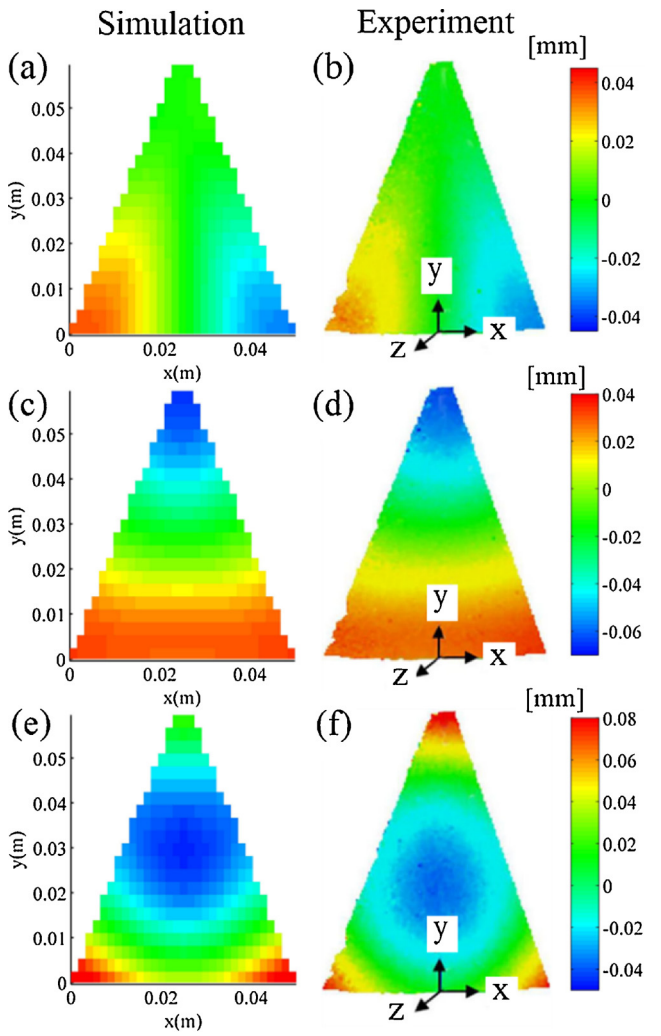


**Fig. 11. Distortion of a horizontally-built prism after being removed from the substrate.** (a), (c) and (e) are *x*, *y* and *z* components of the displacement vector **u** predicted by our model. (b), (d) and (f) are *x*, *y*, and *z* displacement measured with Digital Image Correlation by Wu et al [40] (Reprinted with permission from The Minerals, Metals & Materials Society).

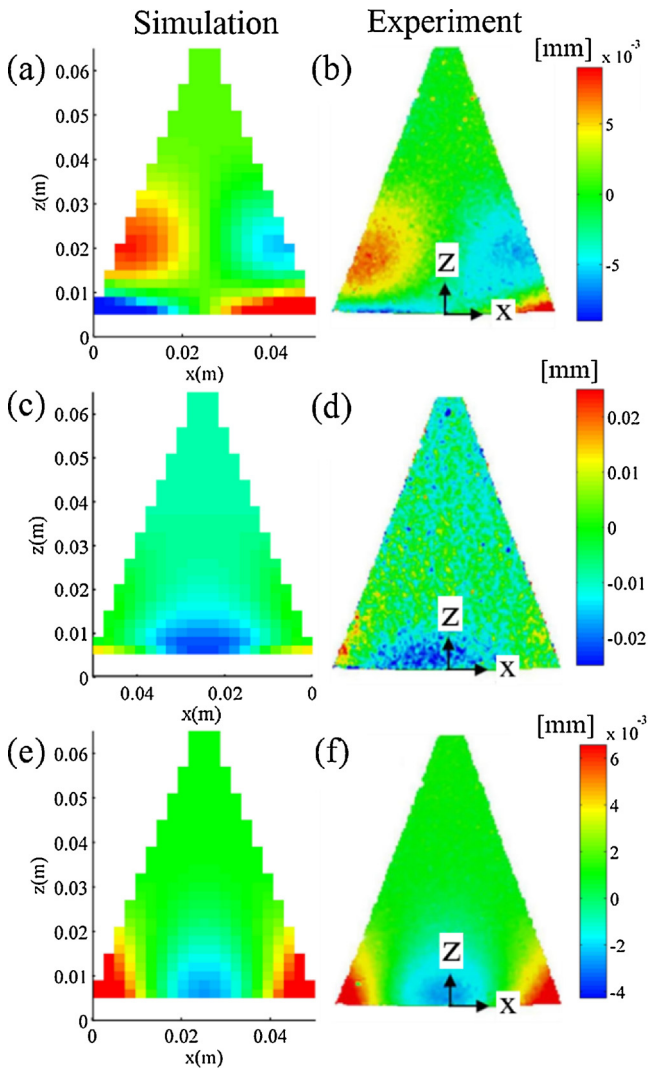


**Fig. 12. Distortion of a vertically-built prism after being removed from the substrate.** (a), (c) and (e) are *x*, *y* and *z* components of the displacement vector **u** predicted by our model. (b), (d) and (f) are *x*, *y*, and *z* displacement measured with Digital Image Correlation by Wu et al [40] (Reprinted with permission from The Minerals, Metals & Materials Society).

and predicted residual stress for $\sigma_{yy}$. However, the match between the experimental and predicted residual stress for $\sigma_{xx}$ and $\sigma_{zz}$ is poor. As the data from Wu et al. [40] was collected from of a different group and on a different machine from our study, we cannot postulate that potential source of deviation; we are reporting our prediction, despite the poor match, for the sake of robust validation and full disclosure of results. It is worth noting that the predicted residual stress profiles $\sigma_{xx}$, $\sigma_{yy}$ and $\sigma_{zz}$ are consistent with the report that residual stress profile in Metal PBF usually exhibits tensile stress at the top and bottom, and a zone of intermediate compressive stress in the middle [41], as predicted by our model (Fig. 13).

### 5.5. Simulation efficiency

Lastly, our TCN-QTM model generally predicts temperature history and part distortion in Metal PBF on the order of minutes. The total number of elements in each simulation (part and support elements), and the computational time for the TCN and QTM model are listed in Table 3. As shown by the computational time required to solve Case Nos. 8–14, the computational time is primarily driven by the height of the part, hence number of superlayers. Additionally, simulations using 316 L stainless steel material properties take longer to solve than those on AlSi10Mg because 316 L stainless steel induces larger thermal stress and consequently requires NR iterations to converge.

## 6. Conclusion and future studies

This manuscript detailed the second part of a combined temperature prediction (thermal circuit network (TCN) in part 1 [1]) and quasi-static thermal mechanical (QTM) model to predict part distortion and residual stress in parts printed by metal powder bed fusion (PBF). Furthermore, the model simulates the support-removal process, and hence both on-substrate and off-substrate displacement and residual stress can be predicted. The TCN-QTM model is validated against experimental data of disk samples with different dimensions and build orientations, demonstrating a relative error less than 20% in terms of radius of curvature at the top surface of the disks and an agreement in the trends of the residual stress. Moreover, the distorted shapes of horizontally- and vertically built prisms predicted by the QTM model both qualitatively and quantitatively match the distortion measured by Wu et al [40]. The combined TCN-QTM model is very fast in comparison to existing Metal PBF prediction algorithms, providing predictions on the order of ten minutes; the ability to provide a computationally

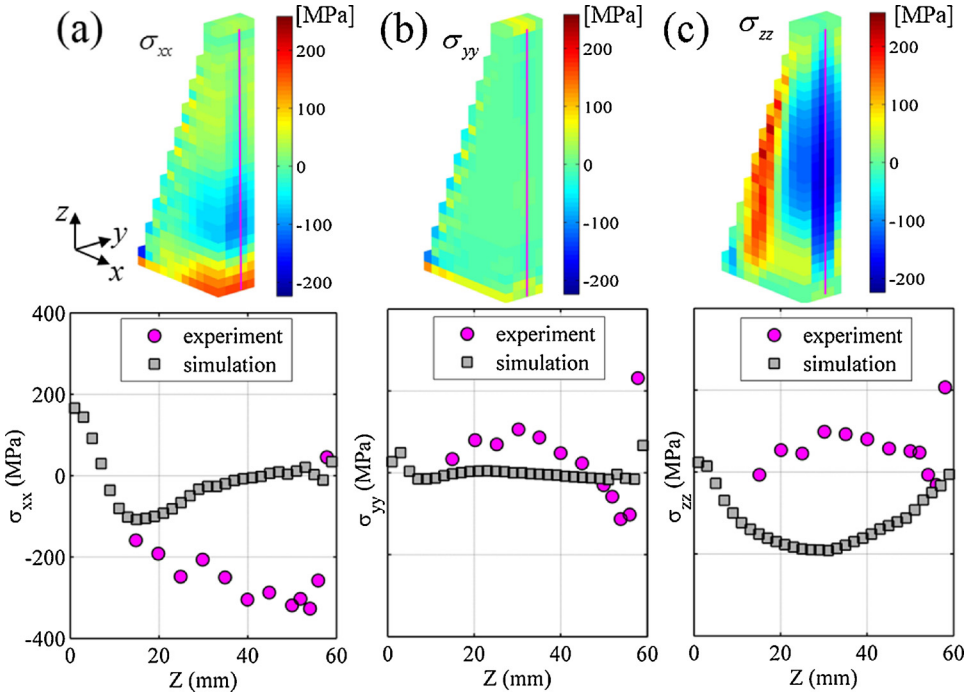


**Fig. 13.** Residual stress in the vertically-built prism after being removed from the substrate predicted by the TCN-QTM model (Only stress in the left half of the prism are shown due to symmetry) and the comparison to stress measured by Wu et al. [40] (The measurement started from $z = 15$ mm. The data were estimated from the paper.): (a) $\sigma_{xx}$, (b) $\sigma_{yy}$, and (c) $\sigma_{zz}$.

**Table 3**
**Computational time for TCN [1] and QTM model.** Case numbers are in reference to Table 2.

| Case No. | Number of Elements | TCN (min) | QTM (min) |
|---|---|---|---|
| 1 | 1456 | 2 | 2.5 |
| 2 | 1456 | 2 | 20 |
| 3 | 3440 | 6 | 25 |
| 4 | 2051 | 2 | 2 |
| 5 | 2688 | 2 | 3 |
| 6 | 3136 | 2 | 3.5 |
| 7 | 3598 | 2 | 4 |
| 8 | 565 | 2 | < 1 |
| 9 | 768 | 2 | < 1 |
| 10 | 960 | 2 | < 1 |
| 11 | 2496 | 2 | 4.5 |
| 12 | 3536 | 2 | 10 |
| 13 | 4224 | 2 | 15 |
| 14 | 6144 | 3 | 70 |
| Horizontal prism | 2842 | 2 | 39 |
| Vertical prism | 2280 | 6 | 23 |

efficient distortion and stress prediction enable future studies into part orientation and support design optimization for autonomous process design.

## Acknowledgements and Disclaimer

This material is based on research sponsored by Air Force Research Laboratory under agreement number FA8650-12-2-7230. The U.S. Government is authorized to reproduce and distribute reprints for Governmental purposes notwithstanding any copyright notation thereon. The views and conclusions contained herein are those of the authors and should not be interpreted as necessarily representing the official policies or endorsements, either expressed or implied, of Air Force Research Laboratory or the U.S. Government.

The authors wish to acknowledge the Canadian Neutron Beam Centre, Canadian Nuclear Laboratories, Chalk River for the neutron beam time.

## Appendix A

### *A1. Justificationand Discussion of Abstraction 1*

In practice, the melt pool is 4–8 real layers of material thick [43]. Our chosen superlayer thickness of 1 mm is 20–30 real layers thick, and is larger than a melt pool depth. To better understand the trade-off between computational efficiency and model accuracy, we performed convergence studies with the superlayer thickness being the independent variable (Fig. A1); this is similar to mesh convergence studies using FEM. A superlayer thickness on the order of 1 mm yields a ROC value that is approaching the converged value of ~1250 mm, but still requires on the order of ten minutes of computation time. Further, reducing the superlayer thickness by an order of magnitude to 0.125 mm increases the computation time by an order of magnitude, which is an unacceptable tradeoff for the intended use of our TCN/QTM model in an optimization algorithm. In addition, the superlayer abstraction, Abstraction 1, has been employed by a number of other Metal PBF models [44,57,58]. A superlayer thickness of 0.5 mm is used by [25], 1 mm by [37], and 2 mm by [44], and thus our superlayer thickness of 1 mm is consistent with common practice.

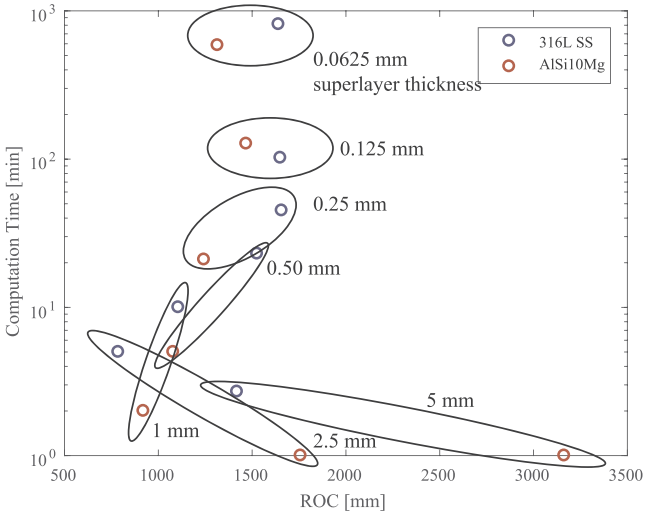


**Fig. A1.** Tradeoff between ROC convergence and computational time for different superlayer thicknesses for 316 L Stainless Steel and AlSi10Mg. Computation time is on a log scale.

**Table A1**
Mechanical properties of AlSi10Mg.

| Temperature (°C) | Yield stress (MPa) | Young's modulus (GPa) |
|---|---|---|
| 25 | 235 | 88.6 |
| 150 | 221 | 86.5 |
| 205 | 194 | 76.1 |
| 260 | 159 | 72.7 |
| 315 | 124 | 62.3 |
| 370 | 90 | 55.4 |
| 427 | 49 | – |

### *A2. Justificationand Discussion of Abstraction 2*

It is well-known that scanning strategy drastically influences the stress field at each layer [58–61]. In particular, if the same scanning pattern is used for each layer, the thermal stress will accumulate along a specific direction, driving larger distortion along that direction [58]. Accordingly, many of the leading Metal PBF machine manufacturers rotate the scan pattern layer to layer to average out the influence of scan pattern over the entire part; for instance, the EOS system used here rotates the scan pattern 67° at each layer. Importantly, there is considerable computational efficiency to be gained by employing Abstraction 2 because there is no need for extremely fine meshes at the melt pool region; given this motivation, other researchers have employed the same assumption [37,45]. Although it is a gross approximation of the real PBF process, we choose to sacrifice prediction accuracy for two orders of magnitude improvement in computational efficiency. Our experiments detailed in Section 5 agree well with our predictions, and similar models that employ Abstraction 2 have also demonstrated a match between the model predictions and experimental results [37,45].

**Table A2**
Mechanical properties of 316 L stainless steel.

| Temperature (°C) | Yield stress (MPa) | Young's modulus (GPa) |
|---|---|---|
| 27 | 290 | 193 |
| 149 | 201 | 190 |
| 260 | 172 | 181 |
| 371 | 159 | 172 |
| 482 | 148 | 162 |
| 593 | 140 | 153 |
| 704 | 131 | 143 |
| 816 | 110 | 132 |

### A3. Material Properties

Temperature dependent material properties and physical properties form AlSi10Mg and 316 L stainless steel are sourced from [62] and [63] (Tables A1–A3).

**Table A3**
Physical properties of AlSi10Mg and 316 L stainless steel.

| Properties | AlSi10Mg | 316 L |
|---|---|---|
| Density (kg/m$^3$) | 2670 | 8000 |
| Thermal conductivity (W/mK) | 111 | 15 |
| Specific heat (J/kgK) | 920 | 500 |
| Thermal expansion coefficient ($10^{-6}$/K) | 19 | 16.5 |
| Solidus temperature (°C) | 580 | 1375 |
| Liquidus temperature (°C) | 780 | 1400 |
| Latent heat (kJ/kg) | 398 | 272.5 |

## References


[1] H. Peng, M. Ghasri-Khouzani, S. Gong, R. Attardo, P. Ostiguy, B. Aboud Gatrell, J. Budzinski, C. Tomonto, J. Neidig, M.R. Shankar, R. Billo, D.B. Go, D.J. Hoelzle, Fast prediction of thermal distortion in metal powder bed fusion additive manufacturing; Part 1: a thermal circuit network model, Submitt. Addit. Manuf. (2017).

[2] Standard Terminology for Additive Manufacturing Technologies, (2015) Withdrawn 2015.

[3] W. Frazier, Metal additive manufacturing: a review, J. Mater. Eng. Perform. 23 (2014) 1917–1928, http://dx.doi.org/10.1007/s11665-014-0958-z.

[4] D.D. Gu, W. Meiners, K. Wissenbach, R. Poprawe, Laser additive manufacturing of metallic components: materials, processes and mechanisms, Int. Mater. Rev. 57 (2012) 133–164, http://dx.doi.org/10.1179/1743280411y.0000000014.

[5] I. Gibson, D.W. Rosen, B. Stucker, Additive Manufacturing Technologies: Rapid Prototyping to Direct Digital Manufacturing, Springer, US, 2009.

[6] K.P. Karunakaran, A. Bernard, S. Suryakumar, L. Dembinski, G. Taillandier, Rapid manufacturing of metallic objects, Rapid Prototyp. J. 18 (2012) 264–280, http://dx.doi.org/10.1108/13552541211231644.

[7] L.E. Murr, S.M. Gaytan, D.A. Ramirez, E. Martinez, J. Hernandez, K.N. Amato, P.W. Shindo, F.R. Medina, R.B. Wicker, Metal fabrication by additive manufacturing using laser and electron beam melting technologies, J. Mater. Sci. Technol. 28 (2012) 1–14, http://dx.doi.org/10.1016/s1005-0302(12)60016-4.

[8] B. Vayre, F. Vignat, F. Villeneuve, Metallic additive manufacturing: state-of-the-art review and prospects, Mech. Ind. 13 (2012) 89–96, http://dx.doi.org/10.1051/meca/2012003.

[9] X. Gong, T. Anderson, K. Chou, Review on powder-based electron beam additive manufacturing technology, Manuf. Rev. 1 (2014) 2, http://dx.doi.org/10.1051/mfreview/2014001.

[10] M. Shellabear, O. Nyrhilä, DMLS-Development history and state of the art Erlangen, Germany, LANE 2004 Conf. (2004).

[11] H.M. Chae, A Numerical and Experimental Study for Residual Stress Evolution in Low Alloy Steel During Laser Aided Additive Manufacturing Process, Ph.D. Thesis in Mechanical Engineering, University of Michigan, 2013.

[12] W. King, A.T. Anderson, R.M. Ferencz, N.E. Hodge, C. Kamath, S.A. Khairallah, Overview of modelling and simulation of metal powder bed fusion process at Lawrence Livermore national laboratory, Mater. Sci. Technol. 31 (2015) 957–968, http://dx.doi.org/10.1179/1743284714Y.0000000728.

[13] N.P. Lavery, S.G.R. Brown, J. Sienz, J. Cherry, F. Belblidia, A review of computational modelling of additive layer manufacturing-multi-scale and multi-physics Cardiff, Wales, UK, Int. Conf. Sustain. Des. Manuf. (2014).

[14] M. Megahed, H.-W. Mindt, N. N'Dri, H. Duan, O. Desmaison, Metal additive-manufacturing process and residual stress modeling, Integrating Mater. Manuf. Innov. 5 (2016) 1–33, http://dx.doi.org/10.1186/s40192-016-0047-2.

[15] P. Aggarangsi, J.L. Beuth, Localized preheating approaches for reducing residual stress in additive manufacturing Austin, TX, Solid Free. Fabr. Symp. (2006).

[16] D. Buchbinder, W. Meiners, N. Pirch, K. Wissenbach, J. Schrage, Investigation on reducing distortion by preheating during manufacture of aluminum components using selective laser melting, J. Laser Appl. 26 (2014) 012004, http://dx.doi.org/10.2351/1.4828755.

[17] N. Shen, K. Chou, Numerical thermal analysis in electron beam additive manufacturing with preheating effects Austin, TX, 23rd Annu. Int. Solid Free. Fabr. Symp. (2012).

[18] I. Yadroitsava, I. Yadroitsev, Residual stress in metal specimens produced by direct metal laser sintering, Solid Free. Fabr. Symp. (2015).

[19] K. Zeng, Optimization of Support Structures for Selective Laser Melting, Ph.D. Thesis in Industrial Engineering, University of Louisville, 2015.

[20] O. Poyraz, E. Yasa, G. Akbulut, A. Orhangul, S. Pilatin, Investigation of support structures for direct metal laser sintering (DMLS) of In625 parts, Annu. Int. Solid Free. Fabr. Symp. (2015).

[21] J.-P. Järvinen, V. Matilainen, X. Li, H. Piili, A. Salminen, I. Mäkelä, O. Nyrhilä, Characterization of effect of support structures in laser additive manufacturing of stainless steel, Phys. Procedia. 56 (2014) 72–81, http://dx.doi.org/10.1016/j.phpro.2014.08.099.

[22] F. Calignano, Design optimization of supports for overhanging structures in aluminum and titanium alloys by selective laser melting, Mater. Des. 64 (12) (2014) 203–213, http://dx.doi.org/10.1016/j.matdes.2014.07.043.

[23] A. Hussein, L. Hao, C. Yan, R. Everson, P. Young, Advanced lattice support structures for metal additive manufacturing, J. Mater. Process. Technol. 213 (2013) 1019–1026, http://dx.doi.org/10.1016/j.jmatprotec.2013.01.020.

[24] T.A. Krol, M.F. Zaeh, C. Seidel, Optimization of supports in metal-based additive manufacturing by means of finite element models Austin, TX, Solid Free. Fabr. Symp. (2012).

[25] T.A. Krol, M.F. Zah, J. Schilp, C. Seidel, C. Groth, Computational-Efficient design of support structures and material modeling for metal-based additive manufacturing, Proc. ANSYS Conf. 29th CADFEM Users Meet. (2011).

[26] S. Ford, Additive Manufacturing Technology: Potential Implications for U.S. Manufacturing Competitiveness, Social Science Research Network, Rochester, NY, 2014.

[27] W.J. Seufzer, NASA Langley Research Center, Additive Manufacturing Modeling and Simulation A Literature Review for Electron Beam Free Form Fabrication, (2014).

[28] Measurement Science Roadmap for Metal-Based Additive Manufacturing, National Institute of Standards and Technology, 2013.

[29] E.R. Denlinger, J. Irwin, P. Michaleris, Thermomechanical modeling of additive manufacturing large parts, J. Manuf. Sci. Eng. 136 (2014), http://dx.doi.org/10.1115/1.4028669 061007–061007.

[30] N.E. Hodge, R.M. Ferencz, J.M. Solberg, Implementation of a thermomechanical model for the simulation of selective laser melting, Comput. Mech. 54 (2014) 33–51, http://dx.doi.org/10.1007/s00466-014-1024-2.

[31] D. Pal, N. Patil, K. Zeng, B. Stucker, An integrated approach to additive manufacturing simulations using physics based, coupled multiscale process modeling, J. Manuf. Sci. Eng. 136 (2014) 061022-1-061022-16.

[32] R. Paul, S. Anand, F. Gerner, Effect of thermal deformation on part errors in metal powder based additive manufacturing processes, J. Manuf. Sci. Eng. 136 (2014), http://dx.doi.org/10.1115/1.4026524 031009–031009.

[33] A. Hussein, L. Hao, C. Yan, R. Everson, Finite element simulation of the temperature and stress fields in single layers built without-support in selective laser melting, Mater. Des. 52 (2013) 638–647, http://dx.doi.org/10.1016/j.matdes.2013.05.070.

[34] K. Dai, L. Shaw, Thermal and mechanical finite element modeling of laser forming from metal and ceramic powders, Acta Mater. 52 (2004) 69–80, http://dx.doi.org/10.1016/j.actamat.2003.08.028.

[35] N. Keller, V. Ploshikhin, New method for fast predictions of residual stress and distortion of AM parts Austin, Texas, Solid Free. Fabr. Symp. (2014).

[36] E.R. Denlinger, J.C. Heigel, P. Michaleris, Residual stress and distortion modeling of electron beam direct manufacturing Ti-6Al-4V, Proc. Inst. Mech. Eng. Part B J. Eng. Manuf. 229 (2014) 1803–1813, http://dx.doi.org/10.1177/0954405414539494.

[37] M.F. Zaeh, G. Branner, Investigations on residual stresses and deformations in selective laser melting, Prod. Eng. 4 (2010) 35–45, http://dx.doi.org/10.1007/s11740-009-0192-y.

[38] L. Zhang, P. Michaleris, P. Marugabandhu, Evaluation of applied plastic strain methods for welding distortion prediction, J. Manuf. Sci. Eng. 129 (2007) 1000, http://dx.doi.org/10.1115/1.2716740.

[39] C. Li, C.H. Fu, Y.B. Guo, F.Z. Fang, Fast prediction and validation of part distortion in selective laser melting, Procedia Manuf. 1 (2015) 355–365, http://dx.doi.org/10.1016/j.promfg.2015.09.042.

[40] A.S. Wu, D.W. Brown, M. Kumar, G.F. Gallegos, W.E. King, An experimental investigation into additive manufacturing-induced residual stresses in 316L stainless steel, Metall. Mater. Trans. A 45 (2014) 6260–6270, http://dx.doi.org/10.1007/s11661-014-2549-x.

[41] P. Mercelis, J.P. Kruth, Residual stresses in selective laser sintering and selective laser melting, Rapid Prototyp. J. 12 (2006) 254–265.

[42] I. Yadroitsev, I. Yadroitsava, Evaluation of residual stress in stainless steel 316L and Ti6Al4V samples produced by selective laser melting, Virtual Phys. Prototyp. 10 (2015) 67–76, http://dx.doi.org/10.1080/17452759.2015.1026045.

[43] W.E. King, H.D. Barth, V.M. Castillo, G.F. Gallegos, J.W. Gibbs, D.E. Hahn,

C. Kamath, A.M. Rubenchik, Observation of keyhole-mode laser melting in laser powder-bed fusion additive manufacturing, J. Mater. Process. Technol. 214 (2014) 2915–2925, http://dx.doi.org/10.1016/j.jmatprotec.2014.06.005.
[44] T.A. Krol, C. Seidel, J. Schilp, M. Hofmann, W. Gan, M.F. Zaeh, Verification of structural simulation results of metal-based additive manufacturing by means of neutron diffraction, Phys. Procedia. 41 (2013) 849–857, http://dx.doi.org/10.1016/j.phpro.2013.03.158.
[45] L. Papadakis, A. Loizou, J. Risse, S. Bremen, J. Schrage, A computational reduction model for appraising structural effects in selective laser melting manufacturing: a methodical model reduction proposed for time-efficient finite element analysis of larger components in selective laser melting, Virtual Phys. Prototyp. 9 (2014) 17–25, http://dx.doi.org/10.1080/17452759.2013.868005.
[46] N. Keller, F. Neugebauer, H. Xu, V. Ploshikhin, Thermo-mechanical simulation of ALM of titanium aerospace structures, Proc. DGM Light., Deutsche Gesellschaft für Materialkunde e. V. (2013).
[47] K. Subburaj, S. Patil, B. Ravi, Voxel-based thickness analysis of intricate objects, Int. J. CAD CAM. 6 (2006) 105–115.
[48] G. Strano, L. Hao, R.M. Everson, K.E. Evans, A new approach to the design and optimisation of support structures in additive manufacturing, Int. J. Adv. Manuf. Technol. 66 (2013) 1247–1254, http://dx.doi.org/10.1007/s00170-012-4403-x.
[49] L.E. Murr, S.M. Gaytan, F. Medina, H. Lopez, E. Martinez, B.I. Machado, D.H. Hernandez, L. Martinez, M.I. Lopez, R.B. Wicker, J. Bracke, Next-generation biomedical implants using additive manufacturing of complex, cellular and functional mesh arrays, Philos. Trans. R. Soc. Math. Phys. Eng. Sci. 368 (2010) 1999–2032, http://dx.doi.org/10.1098/rsta.2010.0010.
[50] L. Cheng, P. Zhang, E. Biyikli, J. Bai, S. Pilz, A.C. To, Integration of topology optimization with efficient design of additive manufactured cellular structures Austin, TX, Proc. Solid Free. Fabr. Symp. (2015).
[51] M.F. Ashby, The properties of foams and lattices, Philos. Trans. Math. Phys. Eng. Sci. 364 (2006) 15–30, http://dx.doi.org/10.1098/rsta.2005.1678.
[52] R.I. Borja, Plasticity: Modeling & Computation, Springer, Berlin Heidelberg, 2013.
[53] P.F. Pai, Highly Flexible Structures: Modeling, Computation, and Experimentation, American Institute of Aeronautics and Astronautics, 2007.
[54] J.C. Simo, R.L. Taylor, Consistent tangent operators for rate-independent elastoplasticity, Comput. Methods Appl. Mech. Eng. 48 (1985) 101–118, http://dx.doi.org/10.1016/0045-7825(85)90070-2.
[55] N.H. Kim, Introduction to Nonlinear Finite Element Analysis, Springer, US, 2014.
[56] M. Ghasri-Khouzani, H. Peng, R. Rogge, R. Attardo, P. Ostiguy, J. Neidig, R. Billo, D. Hoelzle, M.R. Shankar, Experimental measurement of residual stress and distortion in additively manufactured stainless steel components with various dimensions, Mater. Sci. Eng. A 707 (2017) 689–700, http://dx.doi.org/10.1016/j.msea.2017.09.108.
[57] T.A. Krol, S. Westhäuser, M.F. Zäh, J. Schilp, G. Groth, Development of a simulation-based process chain – strategy for different levels of detail for the preprocessing definitions, SNE Simul. Notes Eur. 21 (2011) 135–140, http://dx.doi.org/10.11128/sne.21.tn.10081.
[58] M.F. Zaeh, G. Branner, Investigations on residual stresses and deformations in selective laser melting, Prod. Eng. 4 (2010) 35–45, http://dx.doi.org/10.1007/s11740-009-0192-y.
[59] M.A. Groeber, E. Schwalbach, S. Donegan, K. Chaput, T. Butler, J. Miller, Application of characterization, modelling, and analytics towards understanding process-structure linkages in metallic 3D printing, IOP Conf. Ser. Mater. Sci. Eng. 219 (2017) 012002, http://dx.doi.org/10.1088/1757-899X/219/1/012002.
[60] C. Li, C.H. Fu, Y.B. Guo, F.Z. Fang, Fast prediction and validation of part distortion in selective laser melting, Procedia Manuf. 1 (2015) 355–365, http://dx.doi.org/10.1016/j.promfg.2015.09.042.
[61] N. Keller, V. Ploshikhin, New method for fast predictions of residual stress and distortion of AM parts Austin, TX, Proc. Solid Free. Fabr. Symp. (2014).
[62] NASA, 398 Material Properties Data Sheet, NASA, 2001.
[63] High-temperature Characteristics of Stainless Steels, Committee of Stainless Steel Producers, American Iron and Steel Institute, 1979.